

# Role of Fragility of the Glass Formers in the Yielding Transition under Oscillatory Shear

Roni Chatterjee,<sup>1</sup> Monoj Adhikari,<sup>1</sup> and Smarajit Karmakar<sup>1</sup>

<sup>1</sup>Tata Institute of Fundamental Research, 36/P, Gopanpally Village,  
Serilingampally Mandal, Ranga Reddy District, Hyderabad 500046, Telangana, India

We study the effect of the fragility of glass formers on the yielding transition under oscillatory shear via extensive computer simulations. Employing sphere assemblies interacting with a harmonic potential as our model glass former, we tune fragility by changing the system's density — higher density corresponds to large fragility. Our study reveals significant differences in the yielding transition between strong and fragile glass formers. While both glass formers exhibit similar behaviour for poorly annealed initial conditions, the yielding transition shifts to larger values with increased annealing for fragile glasses while remaining relatively constant for strong glasses. We rationalize our results by introducing a new elastoplastic model, which qualitatively reproduces the simulation results and offers valuable insight into the physics of yielding transition under oscillatory shear deformation.

**Introduction:** Understanding the mechanical behavior of amorphous solids is crucial due to its enormous applications ranging from bulk to nanoscales [1–4] in our day-to-day life. Specifically, the study of amorphous solids under external shear deformation has drawn significant interest in designing better materials for future applications in recent years. Among these, a large number of studies focus on comprehending the response of amorphous solids to uniform shear deformation [5–13]. At small amplitude deformations, the response closely resembles that of crystalline solids; however, under large deformation, numerous plastic deformations occur, eventually leading to yielding and the system starts to flow. Although the nature of the yielding transition is a subject of debate [14–17], energy, or stress shows a discontinuity when driven by oscillatory shear deformation at the yielding transition [18–22].

Recent investigations using cyclic shear predominantly under athermal quasi-static (AQS) conditions indicate that the yielding transition depends on the initial sample's degree of annealing or inherent structure energy. In poorly annealed systems, stroboscopic energy decreases with increasing amplitude of deformation until the yielding amplitude, after which it increases again. Near yielding, the system undergoes an absorbing to diffusing transition: for smaller amplitudes below yielding, the system reaches a steady state called the absorbing state with an invariant stroboscopic configuration; for amplitudes larger than yielding, the steady states are diffusing states where the configuration keeps changing with the number of cycles. This scenario changes significantly if the systems are sufficiently annealed so that the initial energy is below a threshold energy, shown to be the energy at the Mode Coupling Transition temperature [23, 24]. The energy of the system remains constant until reaching the yielding amplitude, where it undergoes a sudden increase and reaches the diffusive states. A similar discontinuous jump in energy is also observed under uniform shear as well [24, 25]. This effect of annealing on yielding is robust across various model systems [25–31], different driving protocols [32, 33], finite temperature, finite shear rate [34, 35], and different dimensions [34, 36, 37].

For poorly annealed glasses, the stress vs. strain curve exhibits a monotonic trend, and the transition to a fluid state is smooth or gradual, particularly under uniform shear condi-

tions. Under cyclic shear, the yielding point is more precisely defined. However, in both cases, material failure resembles ductile behavior. As the degree of annealing increases, a large discontinuous stress drop is observed at yielding in both uniform and cyclic shear, indicating an abrupt and catastrophic transition, characteristic of brittle behavior. The observation of two distinct yielding behaviors, solely by adjusting the degree of annealing, which correlates with the temperature at which the liquid is prepared, raises questions about the existence of a potential phase transition. To answer these questions, various coarse-grained models have been introduced [25, 27, 38–44], which successfully reproduce the observed behaviour in simulation and also attempt to answer the existence of the phase transition. While many of these models support the notion of a phase transition distinguishing between brittle and ductile yielding, the question of its persistence in the thermodynamic limit remains a topic of ongoing debate.

All these studies on yielding described above primarily focused on the initial energy of the system, providing limited insights into the nature of the initial glass former, particularly its fragility, which is a crucial parameter for glass-forming liquids as it connects to various dynamical and structural properties such as dynamical heterogeneity, configurational entropy, violation of the Stokes-Einstein relation, glass forming ability and so on [45–50]. In this article, we investigate whether yielding behavior is similar amongst different fragile glass formers. Through extensive computer simulations, we illustrate that the nature of the yielding transition can vary depending on the fragility of the initial glass. Additionally, we introduce an elastoplastic model that successfully reproduces the simulation results. The analysis of this model allows us to rationalize the observed changes in yielding behavior, attributing them to changes in energy barriers with the annealing history.

**Simulation details:** We investigate a binary mixture (50 : 50) of particles that interact via harmonic potential given by [49, 51]:

$$V_{\alpha\beta}(r) = \frac{\epsilon_{\alpha\beta}}{2} \left(1 - \frac{r}{\sigma_{\alpha\beta}}\right)^2, \quad r_{\alpha\beta} \leq \sigma_{\alpha\beta}$$
$$= 0, \quad r_{\alpha\beta} > \sigma_{\alpha\beta} \quad (1)$$

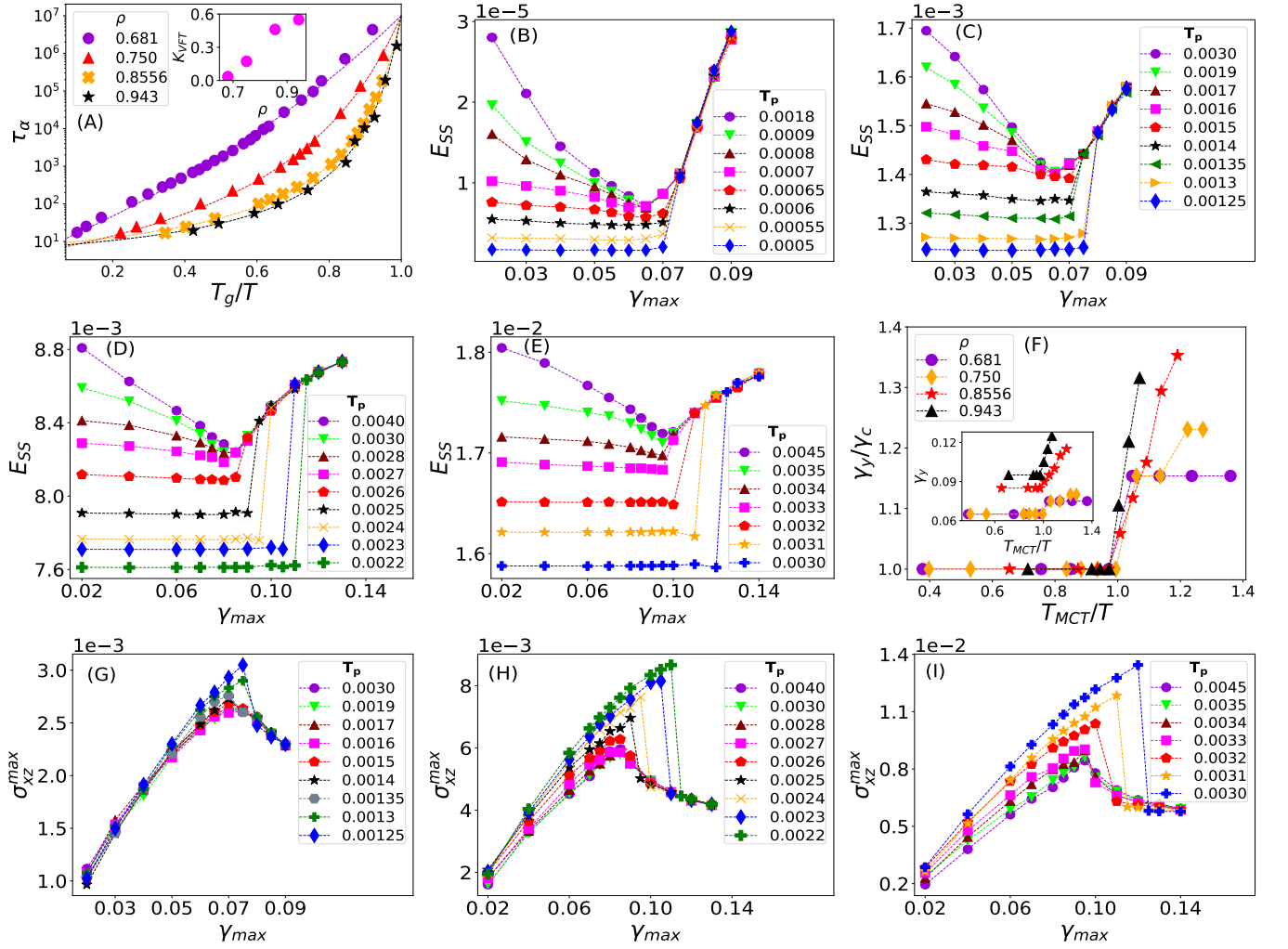


FIG. 1: **Oscillatory Shear Yielding Diagram:** (A) Relaxation time,  $\tau_\alpha$  is plotted as a function of scaled temperature,  $T_g/T$  for all the four studied densities.  $T_g$  is the calorimetric glass transition temperature (see text for definition). The marked variation in the shape of the relaxation curve with changing density highlights the large change in fragility in these systems with increasing density. Inset shows the kinetic fragility as a function of density. (B) Steady-state energy  $E_{SS}$  vs cyclic shear amplitude  $\gamma_{max}$  is plotted for differently annealed samples as indicated by their parent temperatures ( $T_p$ ) for  $\rho = 0.681$ . Notice that the main characteristic of the absence of any mechanical annealing below a critical energy scale along with the nearly no shift in the yield strain ( $\gamma_y$ ) with increasing annealing in this strong glass former. Similar phase diagrams for  $\rho = 0.750$  (C),  $\rho = 0.8556$  (D) and  $\rho = 0.943$  (E) are shown to highlight how yielding transition shifts to higher strain amplitude as the fragility of the glass formers are systematically changed. For most fragile glass former (panel E), the shift in the yield strain at low temperature is very large (nearly 30%). (F) Shows the shifting of  $\gamma_y$  with increasing annealing for all four densities. The x-axis has been scaled by their respective MCT temperature,  $T_{MCT}$  for better comparison. Maximum steady state stress,  $\sigma_{xz}^{max}$ , is plotted against  $\gamma_{max}$  for  $\rho = 0.750$  (G),  $\rho = 0.8556$  (H) and  $\rho = 0.943$  (I), to highlight the stark difference in the yielding transition between strong and fragile glass formers. Strong glass formers continued to show ductile-like yielding with increasing annealing, whereas fragile glass former showed sharp, brittle yielding with increasing annealing as clear from the sharp stress drops across the yielding strain.

where  $\alpha, \beta \in (A, B)$  indicates the type of particle. The two types of particle differ in their size, with  $\sigma_{BB} = 1.4\sigma_{AA}$  (and the diameters are additive), with the interaction strengths being the same for all pairs ( $\epsilon_{AA} = \epsilon_{AB} = \epsilon_{BB}$ ). We have performed simulation at different packing fractions,  $\phi$ , which larger than the  $\phi_J$  as well as  $\phi_0$  [52]. The relation between number density  $\rho$  and packing fraction  $\phi$  for binary mixture

is,

$$\phi = \rho 2^{-d} \frac{\pi^{d/2}}{\Gamma(1 + \frac{d}{2})} (c_A \sigma_{AA}^d + c_B \sigma_{BB}^d) \quad (2)$$

where  $\rho = N/V$ ,  $N$  is the number of particles,  $V$  is the simulation box volume, and  $c_A = c_B = 1/2$ . We have done simulations for  $N = 5000$  particles. We have taken

four packing fractions  $\phi = [0.667, 0.735, 0.8384, 0.925]$  and the corresponding number densities (from Eqs 2)  $\rho = [0.681, 0.750, 0.8556, 0.943]$  to study the effect of fragility on yielding transition. For each density, we equilibrated the samples for a wide range of temperatures, including temperatures well below the Mode Coupling Temperature,  $T_{MCT}$  to study the effect of annealing on yielding ( $T_{MCT}$  are given in the SI). Relaxation time  $\tau_\alpha$  ranges from  $\sim 100$  to  $10^7$  for all the cases.  $\tau_\alpha$  is defined as the time when the two-point correlation function becomes  $q(t = \tau_\alpha) = 1/e$  (the details are shown in the SI). The temperature ranges for  $\rho = 0.681$  is  $T \in (0.0018, 0.0005)$ , for  $\rho = 0.750$  is  $T \in (0.0030, 0.00125)$ , for  $\rho = 0.8556$  is  $T \in (0.0040, 0.0022)$  and for  $\rho = 0.943$  is  $T \in (0.0045, 0.0030)$ . We couldn't achieve  $\tau_\alpha \sim 10^7$  at density  $\rho = 0.943$  due to the crystallisation effect, but we have reached up to  $\tau_\alpha \sim 10^6$ . We have used the conjugate gradient (CG) method on these equilibrated configurations to get the energy-minimised or inherent structure configurations (IS configurations). We then performed cyclic shear on these IS configurations following the AQS protocol. We chose the shear direction as the xz plane. The strain  $\gamma$  varies as  $(0 \rightarrow \gamma_{max} \rightarrow -\gamma_{max} \rightarrow 0)$  indicating a complete cycle, where elementary strain increment,  $d\gamma = 2 \times 10^{-4}$ . For each increment of  $d\gamma$  we performed the following AQS shear protocol - (i) affine transformation of each particle coordinates ( $r_x' \rightarrow r_x + r_z \times d\gamma$ ,  $r_y' \rightarrow r_y$ ,  $r_z' \rightarrow r_z$ ) and then (ii) energy minimisation using CG method. We took 12 independent samples for each temperature of each density. See SI for further details.

**Simulation Results:** In Fig.1A, we show the Angell plot to highlight the large variation of fragility with densities by plotting the relaxation time,  $\tau_\alpha$  against scaled temperature ( $T_g/T$ ). Subsequently, we fit this relaxation time using the Vogel Fulcher Tamannam (VFT) formula:

$$\tau_\alpha = \tau_0 \exp \left[ \frac{1}{K_{VFT}(T/T_{VFT} - 1)} \right], \quad (3)$$

where  $T_{VFT}$  denotes the temperature at which the relaxation time diverges and  $K_{VFT}$  represents the kinetic fragility. We obtain the Angell plot by defining the calorimetric glass transition temperature  $T_g$  such that  $\tau_\alpha(T_g) = 10^7$ . In the inset, we show  $K_{VFT}$  as a function of density. Our observations corroborate with the previous studies that fragility in this soft sphere glass model increases strongly with increasing density [49, 53, 54]. Specifically, the system demonstrates behavior reminiscent of a strong liquid at a density of  $\rho = 0.681$  with  $K_{VFT} \simeq 0.034$ . However, as the density increases, the system becomes more fragile. At the highest density ( $\rho = 0.943$ ),  $K_{VFT} \simeq 0.549$ . Thus, The change in fragility occurred by a factor of around 16, corresponding to a density change of 1.38 times. We then perform cyclic shear in these four glasses at various degrees of annealing as represented by the parent temperatures ( $T_p$ ). Parent temperature refers to the temperature at which the liquid is equilibrated before quenching to zero temperature to prepare the amorphous solid samples. For each chosen cyclic shear amplitude ( $\gamma_{max}$ ), we perform a couple of hundred to thousand cycles of shear deformation until the

energy reaches a steady state value  $E_{SS}$ . Using these extensive cyclic shear simulations, we obtain the yielding diagrams of the systems by plotting  $E_{SS}$  as a function of  $\gamma_{max}$  for all the studied parent temperatures. (Variations of energy with cycles for all the studied systems are shown in the SI). Panels (B), (C), (D) and (E) shows such yielding diagrams for densities  $\rho = 0.681, 0.750, 0.8556$  and  $0.943$  respectively for glass formers exhibiting different fragility. In poorly annealed systems, all glass formers behave similarly: the steady-state energy decreases as  $\gamma_{max}$  increases until reaching the critical yielding point ( $\gamma_Y^c$ ), after which  $E_{SS}$  rises again. For all poorly annealed systems ( $T > T_{MCT}$ ), the systems yield at the same point. We call  $\gamma_Y^c$  critical yield strain because this strain demarcates the difference between the poorly annealed and well-annealed samples. However, stark differences emerge among different glass formers in the well-annealed regime. Although  $E_{SS}$  remains unchanged with increasing  $\gamma_{max}$ , the yielding point shifts to a larger value with increasing annealing for fragile liquids, whereas it remains nearly the same for strong liquids. The yielding point for strong liquids (Fig. 1(B)) occurs more or less at the same point irrespective of the degree of annealing, whereas for the most fragile liquid (Fig. 1(E)), the yielding point shifts to a larger value with increasing annealing below the respective MCT parent temperature ( $T_{MCT}$ ). Just to highlight the changes in the yield strain qualitatively, we estimated the percentage changes in the yield point with respect to the critical yield point and for  $\rho = 0.681$ , the percentage change in yield point is around 15% whereas, for the fragile glass formers, the changes are as large as 35%. These results can provide important insights into observations from previous studies, which we discuss below.

In ref. [24], two model liquids with different fragilities were studied to understand the effect of annealing on yielding. While no direct comparison of yielding transitions was conducted, their data indicates that for the strong liquid silica, the yielding point does not change much with increasing annealing, whereas it shows significant changes for the highly fragile liquid, KA BMLJ. Recent investigations [55, 56] on the shear deformation of active glasses reveal that the yielding point shows minimal change with increasing annealing. Our results indicate that these apparent changes in yielding behavior are closely related to the fragility of the system.

In Fig.1(F), we illustrate  $\gamma_Y/\gamma_Y^c$  as a function of  $T_{MCT}/T$ , where  $\gamma_Y$  denotes the yielding point and  $\gamma_Y^c$  denotes the yielding point of poorly annealed glasses. The yielding point does not change for different glasses until  $T_{MCT}$ ; however, below  $T_{MCT}$  it increases rapidly with increasing fragility, whereas for the strong glasses, it remains almost constant. The inset of Fig. 1(F) shows that for strong glasses, yielding occurs for smaller deformations. These observations lead to the interesting phenomenon that strong glasses yield faster.

To further elucidate the yielding transition under cyclic shear, in Fig.1(G)-(I), we show the maximum steady state stress  $\sigma_{xz}^{max}$  as a function of  $\gamma_{max}$  for different parent temperatures. In the case of strong glass (Fig.1(G)), we observe that for various parent temperatures,  $\sigma_{xz}^{max}$  increases as  $\gamma_{max}$  increases until it reaches the yield point. Interestingly, the yield points appear to be similar across different parent tem-

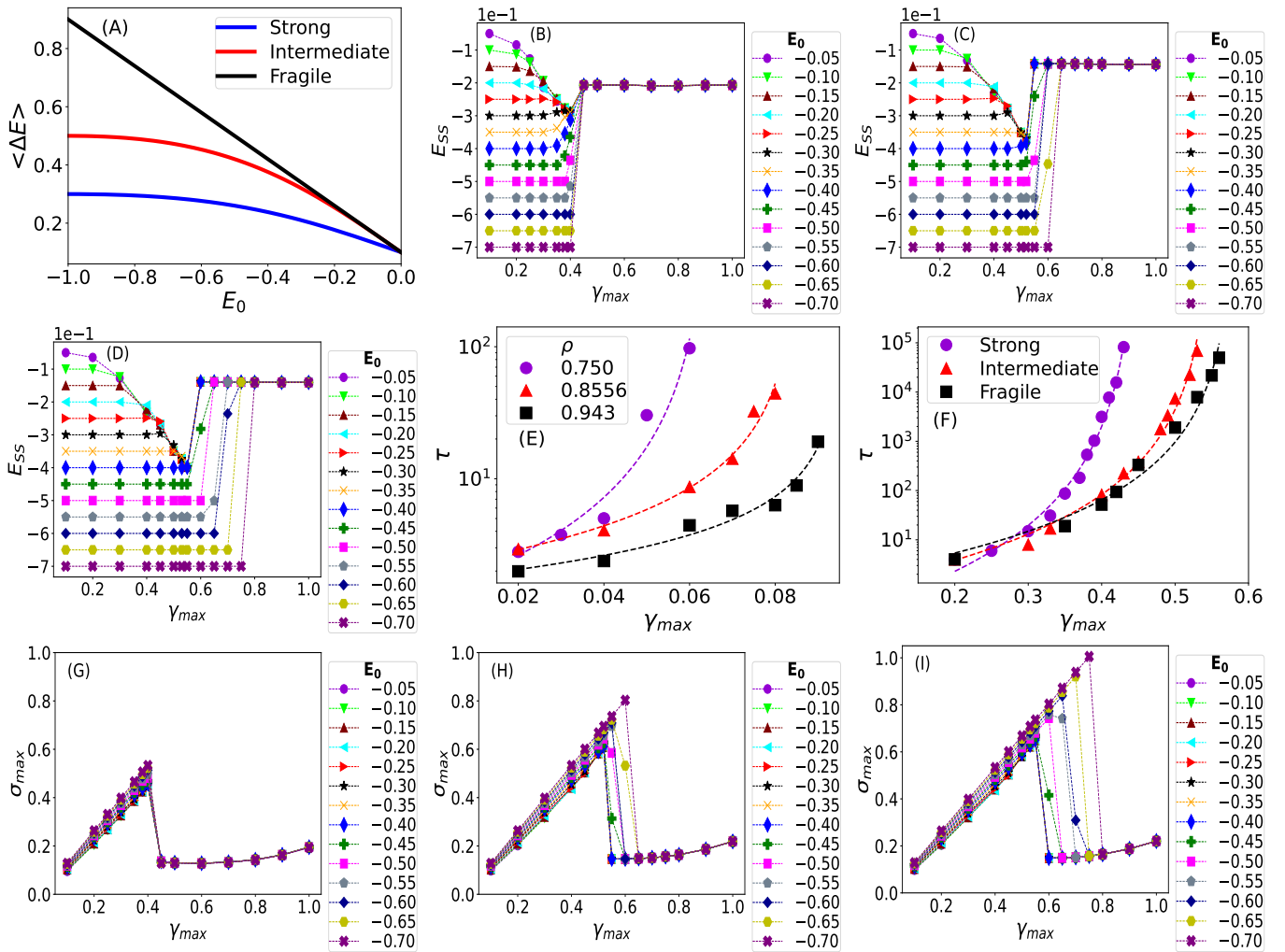


**FIG. 2: Mesoscale Elastoplastic Model:** (A) Schematic of Mean barrier as a function inherent state energy  $E_0$  following Eq.6 and Eq. 7. (B) Steady-state energy vs  $\gamma_{max}$  for a model strong glass former with energy barrier depicted by the blue curve in panel (A). The energy barrier saturates with increasing annealing (equivalent to more negative inherent structure energy,  $E_0$ ). Note that the poorly annealed states show further annealing with increasing  $\gamma_{max}$ , but for better-annealed states, there is no annealing and yield strain does not increase. (C) A similar yielding diagram for a model system with intermediate fragility is depicted in panel (A) by a red curve. In this case, the poorly annealed part of the diagram shows similar results to the strong glass former but notes the better-annealed part. The yield strain increases with increasing annealing. (D) Shows the results for the most fragile case. The striking difference is the better-annealed part of the yielding diagram. The yield strain increases significantly with increasing annealing in complete agreement with simulation results. (E) Shows the number of cycles needed to reach steady state ( $\tau$ ) vs  $\gamma_{max}$  from simulation for three densities with increasing fragility.  $\tau$  is the smallest for a given  $\gamma_{max}$  for the fragile system with  $\rho = 0.943$ , indicating the ease of reaching a steady state for fragile glass formers. (F) Similar timescale data from the elastoplastic model. Excellent qualitative match with the simulation results is indeed very encouraging. (G)  $\sigma_{max}$  vs  $\gamma_{max}$  plot for strong glass-former. (H) and (I) show a stress-strain curve for intermediate and fragile scenarios. Again, the qualitative match with the simulation results shown in Fig.1(G)-(H) is very good. See the text for more discussions.

peratures. Subsequently, stress drops to a lower value. This stress-strain behavior not only reaffirms that the yielding point does not change with the degree of annealing but also suggests that strong glasses remain ductile even in the most annealed samples. However, the stress-strain behavior changes significantly for fragile glass (Fig. 1(I)). With increasing annealing, the yielding point shifts to a larger value and becomes brittle for well-annealed glasses with sharp stress drops at the yield-

ing strains. Thus, this result, combined with the yielding diagram described above, reveals that the nature of yielding is highly dependent on the fragility of the glass formers.

**Elastoplastic Mesomodel Results:** We now consider whether the observed phenomena in simulation can be reproduced and the underlying mechanism could be understood using a simple mean-field mesoscopic model. While the understanding of yielding behavior under uniform shear deforma-

tions using a mesoscopic model has been extensively studied [27, 57–59], there is a growing interest in comprehending yielding behavior under cyclic shear deformation recently [38, 40–43, 60, 61]. The main ingredient of many of these models is the assumption of a local energy landscape associated with a volume of material, often referred to as a meso block. However, it is not immediately clear how large a volume one needs to consider for the validity of the assumption. One assumes that each of these blocks of materials can be considered independent from each other, and a collection of such blocks can constitute a macroscopic body of materials. The absence of interactions between blocks can be thought of as a mean-field approximation. Within this approximation, one further assumes that each of these meso-blocks evolves on the energy landscape when subjected to various deformations, such as oscillatory shear deformation. When the block reaches its local yield threshold, it topples to another energy minimum amongst all the accessible minima it has, and the process continues as long as the body is subjected to the deformation. In Ref.[38], it was assumed that such block is associated with an absolute energy minimum  $E_0$  and a strain  $\gamma_0$  (where energy is minimum as a function of strain). The yield threshold is modelled via a stability range of strain ( $\gamma_{\pm}$ ), beyond which the system topples to a new energy minimum. Under strain, a quadratic variation of energy is considered, assuming Hooke's law of linear elasticity. It was further assumed that  $E_0$  follows a Gaussian distribution,

$$P(E_0) = \sqrt{\frac{2}{\pi\sigma^2}} \exp\left(-\frac{E_0^2}{2\sigma^2}\right), \quad (4)$$

where  $-1 < E_0 < 0$ ,  $\sigma = 0.1$  and energy evolution with strain  $\gamma$  is,

$$E(\gamma, E_0, \gamma_0) = E_0 + \frac{\mu}{2}(\gamma - \gamma_0)^2, \quad (5)$$

where  $\mu = 1.1$  and the stability limit is,  $\gamma_{\pm} = \gamma_0 \pm \sqrt{|E_0|}$ . The yielding diagram of this model closely resembles what we observed for fragile glass formers. However, neither this model nor others in the literature [40–43, 60, 61] consider the impact of the initial glass former's fragility on the yielding diagram. However, our simulation results suggest a significant change in the yielding diagram when the fragility of the initial glass former varies. Therefore, we propose a new model similar to the concept discussed in Ref. [38] but with a crucial difference of energy barrier playing a crucial role in plasticity.

Previous studies [54, 62] have shown that the energy barrier ( $\Delta E$ ) of the fragile glass-formers increases strongly with decreasing temperature or increasing annealing, but for strong glass-formers, the energy barrier increases very slowly. We have introduced this crucial aspect of variation of energy barrier with parent temperature or annealing in our version of elastoplastic model. The energy barrier distribution is assumed to be Gaussian, with the mean energy barrier,  $\langle \Delta E \rangle$ , varying with  $E_0$  or parent temperature,  $T_p$ . We have chosen two trial functions for ( $\langle \Delta E \rangle$ ) variation with annealing ( $E_0$ ). For fragile glass-formers, we took

$$\langle \Delta E \rangle = a + b|E_0| \quad (6)$$

and for strong glass-formers

$$\langle \Delta E \rangle = a + b \left( \frac{E_0^2}{1 + E_0^2} \right) \quad (7)$$

with  $a = 0.10$ ,  $b = 0.80$ . A schematic is shown in Fig. 2(A). We propose that the stability limit should depend on the energy barrier ( $\Delta E$ ) as

$$\gamma_{\pm} = \gamma_0 \pm [\Delta E]^{2/3}. \quad (8)$$

The exponent  $2/3$  is used instead of  $1/2$  as it was already shown that the energy barrier vanishes as a power-law with exponent  $2/3$  as the plastic strain is approached [7]. We also considered uniform distribution of  $\gamma_0 \in (-1, 1)$  as in [38]. The cyclic shear in this model goes as follows.

- (i) start with an initial energy minimum  $E_0$  and  $\gamma_0 = 0$ .
- (ii) For this  $E_0$ , get  $\langle \Delta E \rangle$  from the equation 6 or 7 and the corresponding  $\Delta E$  is chosen from Gaussian distribution whose width  $\sigma_{\Delta E}$  decreases linearly from 5% to 0.001% of  $E_0$  with annealing.
- (iii) Define the stability limit using Eq.8.
- (iv) Energy is then varied with strain as  $E(\gamma, E_0, \gamma_0) = E_0 + \frac{\mu}{2}(\gamma - \gamma_0)^2$  until the stability limit is reached.  $\mu$  is increased linearly from 1 to 1.5 with annealing.
- (v) Whenever the system crosses its stability limit  $\gamma_{\pm}$ , it jumps to any lower energy mesostate at the transition strain, and a new set of  $E_0$  and  $\gamma_0$  are chosen from the respective distributions, and we repeat the process from (ii).

The strain  $\gamma$  is varied cyclically with amplitude  $\gamma_{max}$ , and the number of cycles is around 10000. If the zero strain energy of the system doesn't change with successive cycles, the procedure is terminated. The average zero strain energies of the last 500 cycles are calculated to obtain  $E_{SS}$ . We took 100 independent samples for better averaging. We studied the model within the same range of  $E_0 \in (-0.05, -0.70)$  for all the samples.  $E_{SS}$  vs  $\gamma_{max}$  is plotted for all the cases for this elastoplastic model in Fig. 2(B) - (D). As we can see, the yielding point for the strong model barely shifts below the critical energy, while for the fragile model, the shift in yielding point with annealing is very large, in complete agreement with simulation results.

From our modified elastoplastic model, we get additional information about timescales (the number of cycles needed to reach a steady state) for both the strong and fragile glass formers. In Fig. 2(E), we show the timescale obtained from our MD simulations for strong, intermediate and fragile glass-formers. One can clearly see that the number of cycles needed to reach a steady state for a strong glass-former is way larger than fragile glass-formers for a given  $\gamma_{max}$ . We have fitted the zero strain energy (stroboscopic energy) as a function of cycles using a stretched exponential function to find the steady-state energy and the timescale for the most poorly annealed samples for three densities,  $\rho = 0.750, 0.8556, 0.943$ . The

timescales are found to show a power-law-like divergence at the respective critical yield strain  $\gamma_Y^c$ , which shifts to a larger strain as the system becomes more fragile. These simulation outcomes can be qualitatively described by our model also. A detailed characterization of this divergence is shown in the SI.

Next, in Fig. 2(F), we show the results obtained using our elastoplastic model, and remarkable agreement with the simulation results suggests the crucial role played by the energy barrier in modelling these systems even at the mean-field level. In this model, we considered the number of cycles to reach the steady state as the characteristic relaxation timescale, and we found that the power-law divergence exponent is higher for strong glass than the fragile one, again in agreement with the simulation results. In Fig. 2(G)-(I), we show  $\sigma^{max}$  vs  $\gamma_{max}$  as obtained from our elastoplastic model to draw a parallel with the simulations results in Fig. 1(G)-(I). One also sees that for strong liquids, the yield strain does not change much as well and the stress jump is found to be small compared to the fragile ones. In fragile glass-formers, the yield strain changes significantly with annealing, and the corresponding stress drops as the yielding increases, as seen in the simulations. The remarkable agreement between the mean-field elastoplastic model and the simulation results is really encouraging, suggesting that much of the oscillatory shear yielding in a wide variety of amorphous solids might be possible to understand within the mean-field framework. In the future, we plan to extend this model to include spatial dimensions to see whether some of the missing physics can be incorporated into the elastoplastic model.

**Conclusion:** In this study, we show that the fragility of the initial glass former significantly influences the nature of the yielding transition under cyclic shear. Fragility of the glass former is an indicator of how quickly viscosity or relaxation time increases with decreasing temperature in the supercooled liquid temperature regime. Our findings are particularly noteworthy because they reveal how the kinetic properties of liquids can strongly influence the mechanical properties of amorphous solids, providing new insights into the behavior of these materials. Our results reveal that while the yielding response of strong and fragile liquids in their poorly annealed states is similar, a striking difference emerges when they are better annealed. We found that fragile glass formers show a large increase in yielding strain with increasing annealing, while strong glass formers show almost no change in their yielding strain with better annealing. This difference is also apparent in their stress-strain relationship. Strong glass-formers

show nearly ductile yielding with no significant change in the characteristic with increasing annealing, whereas fragile glass-formers show increasingly brittle yielding with increasing annealing, characterized by a very large stress jump at the yield strain.

Additionally, we observe that strong glass formers take significantly more shear cycles to reach an absorbing state when the strain amplitude is below their yield strain, while fragile glass formers reach their absorbing state much faster at the same strain amplitude. These differences are quite intriguing and led us to propose a modified mean-field elastoplastic model that considers the crucial role of energy barriers in amorphous plasticity, which was previously missing in other works. By introducing a temperature-dependent growth of energy barrier, particularly a weakly growing energy barrier for strong glass-formers and a strongly growing energy barrier for fragile glass-formers with temperature, we could explain the simulation's observations with remarkable accuracy. We also found that the yielding diagram under oscillatory shear can be a useful tool for estimating the growth of energy barriers in various glass-formers and may help us better understand their liquid properties. Finally, our results provide insights into how the variation in energy barrier with annealing can affect the mechanical response of amorphous solids under oscillatory shear. We believe our findings will encourage future research to develop a unified description of the mechanical yielding of a wide variety of amorphous solids using mean-field theories while considering energy barriers and their essential role in plasticity.

**Acknowledgements:** We want to thank Srikanth Sastry, Pinaki Chaudhuri, Viswas Venkatesh and Shiladitya Sengupta for many useful discussions. We acknowledge funding by intramural funds at TIFR Hyderabad from the Department of Atomic Energy (DAE) under Project Identification No. RTI 4007. SK acknowledges Swarna Jayanti Fellowship grants DST/SJF/PSA01/2018-19 and SB/SFJ/2019-20/05 from the Science and Engineering Research Board (SERB) and Department of Science and Technology (DST) and the National Super Computing Mission (NSM) grant DST/NSM/R&D\_HPC\_Applications/2021/29 for generous funding. Most of the computations are done using the HPC clusters procured using Swarna Jayanti Fellowship grants DST/SJF/PSA01/2018-19, SB/SFJ/2019-20/05 and Core Research Grant CRG/2019/005373. MA acknowledges support from NSM grant DST/NSM/R&D\_HPC\_Applications/2021/29 for financial support.

- 
- [1] S. M. Fielding, P. Sollich, and M. E. Cates, *Journal of Rheology* **44**, 323 (2000).
  - [2] M. L. Falk and J. S. Langer, *Annu. Rev. Condens. Matter Phys.* **2**, 353 (2011).
  - [3] C. A. Schuh, T. C. Hufnagel, and U. Ramamurty, *Acta Materialia* **55**, 4067 (2007).
  - [4] D. Bonn, M. M. Denn, L. Berthier, T. Divoux, and S. Manneville, *Reviews of Modern Physics* **89**, 035005 (2017).
  - [5] Y. Shi and M. L. Falk, *Physical review letters* **95**, 095502 (2005).
  - [6] Y. Shi, M. B. Katz, H. Li, and M. L. Falk, *Physical review letters* **98**, 185505 (2007).
  - [7] S. Karmakar, E. Lerner, and I. Procaccia, *Physical Review E* **82**, 055103 (2010).
  - [8] S. Karmakar, A. Lemaitre, E. Lerner, and I. Procaccia, *Physical review letters* **104**, 215502 (2010).

- [9] N. C. Keim and P. E. Arratia, *Soft Matter* **9**, 6222 (2013).
- [10] D. V. Denisov, M. T. Dang, B. Struth, A. Zaccone, G. H. Wegdam, and P. Schall, *Scientific Reports* **5** (2015), [10.1038/srep14359](https://doi.org/10.1038/srep14359).
- [11] J. Lin, E. Lerner, A. Rosso, and M. Wyart, *Proceedings of the National Academy of Sciences* **111**, 14382 (2014).
- [12] B. P. Bhowmik, P. Chaudhuri, and S. Karmakar, *Physical review letters* **123**, 185501 (2019).
- [13] A. Barbot, M. Lerbinger, A. Lemaitre, D. Vandembroucq, and S. Patinet, *Physical Review E* **101**, 033001 (2020).
- [14] T. Kawasaki and L. Berthier, *Physical Review E* **94**, 022615 (2016).
- [15] I. Procaccia, C. Rainone, and M. Singh, *Physical Review E* **96**, 032907 (2017).
- [16] P. K. Jaiswal, I. Procaccia, C. Rainone, and M. Singh, *Physical review letters* **116**, 085501 (2016).
- [17] G. P. Shrivastav, P. Chaudhuri, and J. Horbach, *Physical Review E* **94**, 042605 (2016).
- [18] D. Fiocco, G. Foffi, and S. Sastry, *Phys. Rev. E* **88**, 020301 (2013).
- [19] I. Regev, T. Lookman, and C. Reichhardt, *Phys. Rev. E* **88**, 062401 (2013).
- [20] K. H. Nagamanasa, S. Gokhale, A. Sood, and R. Ganapathy, *Physical Review E* **89**, 062308 (2014).
- [21] P. Leishangthem, A. D. Parmar, and S. Sastry, *Nature Communications* **8**, 14653 (2017).
- [22] A. D. Parmar, S. Kumar, and S. Sastry, *Physical Review X* **9**, 021018 (2019).
- [23] W.-T. Yeh, M. Ozawa, K. Miyazaki, T. Kawasaki, and L. Berthier, *Physical review letters* **124**, 225502 (2020).
- [24] H. Bhaumik, G. Foffi, and S. Sastry, *Proceedings of the National Academy of Sciences* **118** (2021).
- [25] M. Ozawa, L. Berthier, G. Biroli, A. Rosso, and G. Tarjus, *Proceedings of the National Academy of Sciences* **115**, 6656 (2018).
- [26] T. Divoux, E. Agoritsas, S. Aime, C. Barentin, J.-L. Barrat, R. Benzi, L. Berthier, D. Bi, G. Biroli, D. Bonn, *et al.*, *arXiv preprint arXiv:2312.14278* (2023).
- [27] H. J. Barlow, J. O. Cochran, and S. M. Fielding, *Physical Review Letters* **125**, 168003 (2020).
- [28] M. Ozawa, Y. Iwashita, W. Kob, and F. Zamponi, *Nature Communications* **14**, 113 (2023).
- [29] N. C. Keim and D. Medina, *Science Advances* **8**, eabo1614 (2022).
- [30] J. Pollard and S. M. Fielding, *Physical Review Research* **4**, 043037 (2022).
- [31] A. Mutneja, B. P. Bhowmik, and S. Karmakar, *arXiv preprint arXiv:2307.01002* (2023).
- [32] V. V. Krishnan, K. Ramola, and S. Karmakar, *Physical Review Applied* **19**, 024004 (2023).
- [33] M. Adhikari, M. Mungan, and S. Sastry, *arXiv preprint arXiv:2201.06535* (2022).
- [34] M. Singh, M. Ozawa, and L. Berthier, *Physical Review Materials* **4**, 025603 (2020).
- [35] K. Lamp, N. Kuchler, and J. Horbach, *The Journal of Chemical Physics* **157** (2022).
- [36] M. Ozawa, L. Berthier, G. Biroli, and G. Tarjus, *Physical Review Research* **2**, 023203 (2020).
- [37] H. Bhaumik, G. Foffi, and S. Sastry, *The Journal of Chemical Physics* **156** (2022).
- [38] S. Sastry, *Physical Review Letters* **126**, 255501 (2021).
- [39] J. T. Parley, S. Sastry, and P. Sollich, *Physical Review Letters* **128**, 198001 (2022).
- [40] K. Khirallah, B. Tyukodi, D. Vandembroucq, and C. E. Maloney, *Phys. Rev. Lett.* **126**, 218005 (2021).
- [41] C. Liu, E. E. Ferrero, E. A. Jagla, K. Martens, A. Rosso, and L. Talon, *The Journal of Chemical Physics* **156** (2022).
- [42] D. Kumar, S. Patinet, C. E. Maloney, I. Regev, D. Vandembroucq, and M. Mungan, *The Journal of Chemical Physics* **157** (2022).
- [43] S. Rossi, G. Biroli, M. Ozawa, G. Tarjus, and F. Zamponi, *Physical Review Letters* **129**, 228002 (2022).
- [44] J. T. Parley and P. Sollich, *arXiv preprint arXiv:2310.07843* (2023).
- [45] S. Sastry, *Nature* **409**, 164 (2001).
- [46] T. Scopigno, G. Ruocco, F. Sette, and G. Monaco, *Science* **302**, 849 (2003).
- [47] G. Ruocco, F. Sciortino, F. Zamponi, C. De Michele, and T. Scopigno, *The Journal of chemical physics* **120**, 10666 (2004).
- [48] H. Tanaka, *Journal of non-crystalline solids* **351**, 678 (2005).
- [49] M. Adhikari, S. Karmakar, and S. Sastry, *The Journal of Physical Chemistry B* **125**, 10232 (2021).
- [50] C. Alba-Simionesco and G. Tarjus, *Journal of Non-Crystalline Solids: X* **14**, 100100 (2022).
- [51] D. J. Durian, *Physical review letters* **75**, 4780 (1995).
- [52] M. Adhikari, S. Karmakar, and S. Sastry, *Physical Review Letters* **131**, 168202 (2023).
- [53] L. Berthier and T. A. Witten, *Europhysics Letters* **86**, 10001 (2009).
- [54] I. Tah, S. A. Ridout, and A. J. Liu, *The Journal of Chemical Physics* **157** (2022).
- [55] R. Sharma and S. Karmakar, *arXiv preprint arXiv:2305.17545v1* (2023).
- [56] Y. Goswami, G. Shivashankar, and S. Sastry, *arXiv preprint arXiv:2312.01459* (2023).
- [57] A. Nicolas, E. E. Ferrero, K. Martens, and J.-L. Barrat, *Reviews of Modern Physics* **90**, 045006 (2018).
- [58] M. Popović, T. W. de Geus, and M. Wyart, *Physical Review E* **98**, 040901 (2018).
- [59] M. Talamali, V. Petäjä, D. Vandembroucq, and S. Roux, *Comptes Rendus Mécanique* **340**, 275 (2012).
- [60] J. T. Parley, S. Sastry, and P. Sollich, (2021), [arXiv:2112.11578 \[cond-mat.soft\]](https://arxiv.org/abs/2112.11578).
- [61] J. O. Cochran, G. L. Callaghan, and S. M. Fielding, *arXiv preprint arXiv:2211.11677* (2022).
- [62] I. Tah and S. Karmakar, *Physical Review Materials* **6**, 035601 (2022).

# Role of Fragility of the Glass Formers in the Yielding Transition under Oscillatory Shear - Supplemental Information

Roni Chatterjee,<sup>1</sup> Monoj Adhikari,<sup>1</sup> and Smarajit Karmakar<sup>1</sup>

<sup>1</sup>Tata Institute of Fundamental Research, 36/P, Gopanpally Village, Serilingampally Mandal, Ranga Reddy District, Hyderabad 500046, Telangana, India

## S1. EQUILIBRATION OF THE LIQUID

As discussed in the main text, our initial configuration before shear deformation starts is obtained by equilibrating the liquid at a given temperature. Below, we show the mean squared displacement (MSD) and overlap function as functions of time to demonstrate that the liquid has reached to equilibrium.

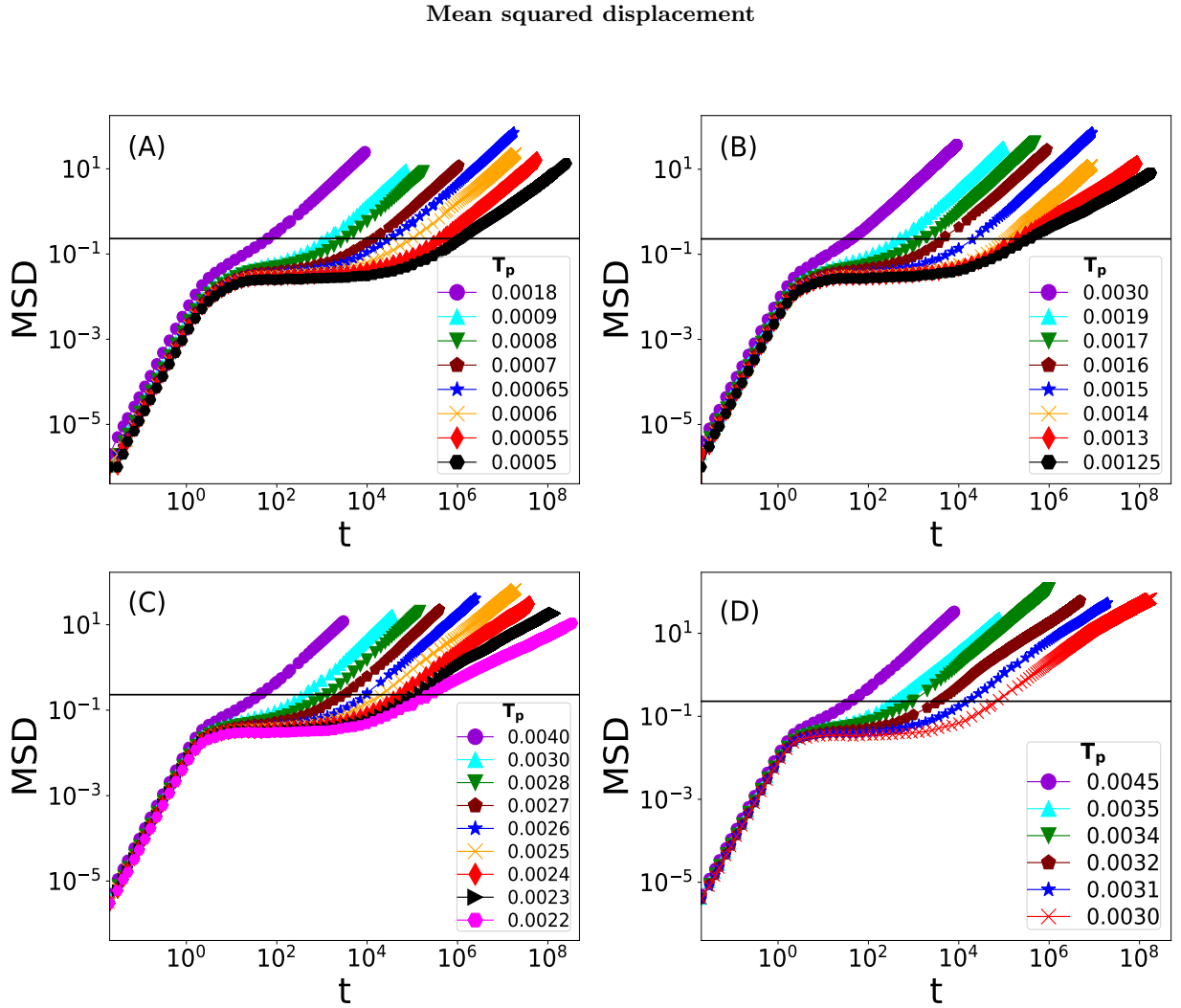


FIG. S1. Plot of mean squared displacement with time  $t$  for system size  $N = 5000$  at different parent temperatures ( $T_p$ ) at densities (A)  $\rho = 0.681$ , (B)  $\rho = 0.750$ , (C)  $\rho = 0.8556$ , (D)  $\rho = 0.943$ . The solid black line corresponds to the cut-off parameter  $a^2 = 0.2304$ .



Mean squared displacement (considering the B-type particles only) is defined as :

$$\Delta r^2(t) = \frac{1}{N_B} \sum_{i=1}^{N_B} |\vec{r}_i(t+t_0) - \vec{r}_i(t_0)|^2, \quad (\text{S1})$$

where  $r_i(t)$  is the position of the  $i$ -th particle at time  $t$ . The Mean Squared Displacement (MSD) is calculated by averaging over 12 samples. We have conducted long MD simulation runs (with a duration of approximately  $10^8$ ) to ensure that the MSD reaches the diffusive region for each temperature. The black line represents the value of the cut-off parameter  $a^2 = 0.2304$ , which we use to compute the overlap function, which is shown next.

### Overlap function

The overlap function  $q(t)$  (considering the B-type particles only) is defined as :

$$q(t) = \frac{1}{N_B} \sum_{i=1}^{N_B} w(|\vec{r}_i(t_0) - \vec{r}_i(t+t_0)|) \quad (\text{S2})$$

where  $w(x) = 1.0$  if  $x \leq a$  and  $= 0$  otherwise. Here  $a = 0.48$  is chosen from the plateau value ( $a^2 = 0.2304$ ) of the MSD curves.  $q(t)$  is calculated by averaging over 12 samples. Again, the decay of  $q(t)$  to zero ensures that we have equilibrated all the liquids at their respective temperatures. The relaxation time ( $\tau_\alpha$ ) is calculated at the time where  $q(t = \tau_\alpha) = \frac{1}{e}$ .

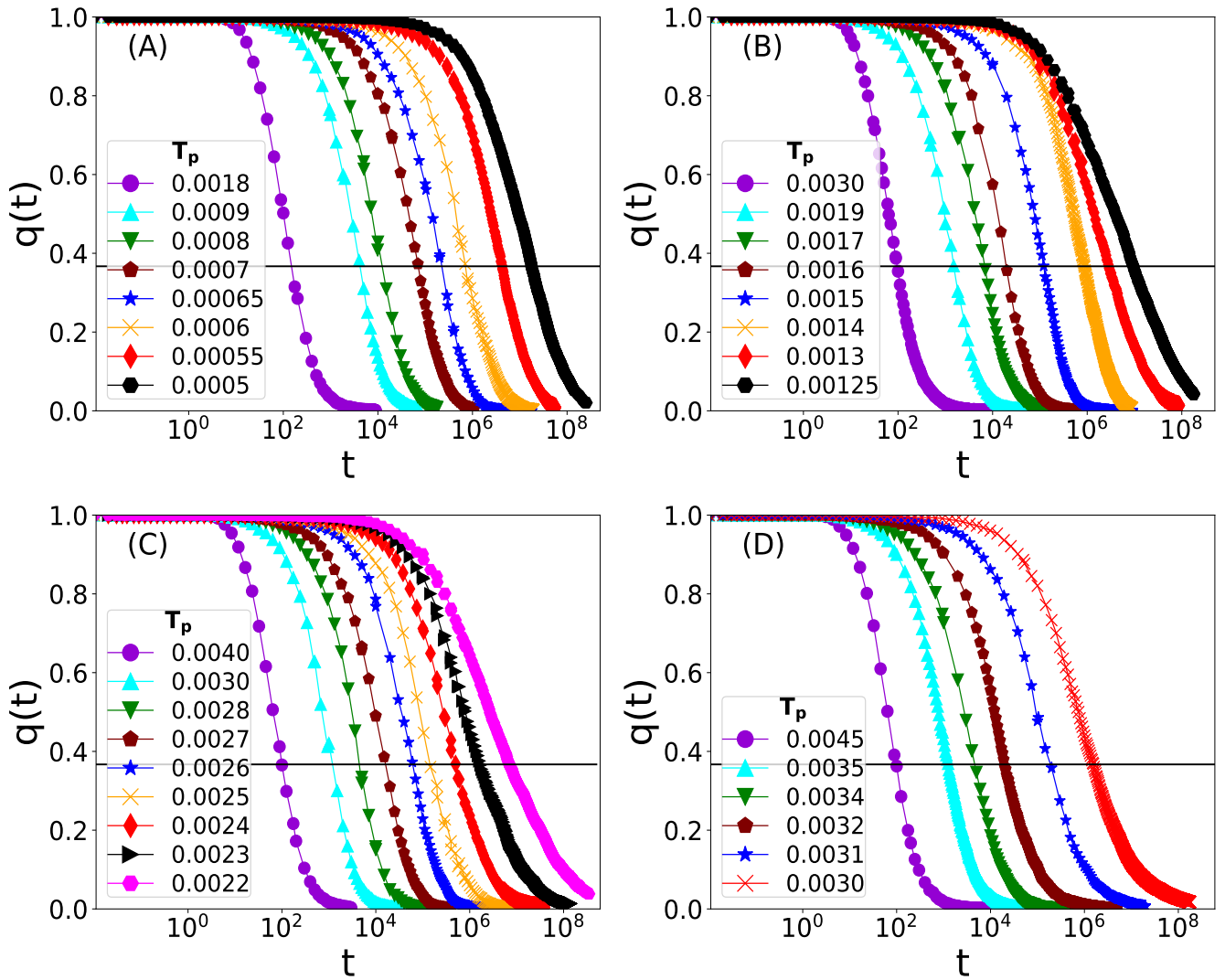


FIG. S2. Plot of overlap function  $q(t)$  with time  $t$  at wide range of parent temperatures ( $T_p$ ) at densities (A)  $\rho = 0.681$ , (B)  $\rho = 0.750$ , (C)  $\rho = 0.8556$ , (D)  $\rho = 0.943$ . The solid black line corresponds to  $q(t = \tau_\alpha) = \frac{1}{e}$ . System size  $N = 5000$  for all panels.

### INHERENT STRUCTURE ENERGY

After equilibration, we achieve the amorphous solid state by minimizing the liquid. We employ the Conjugate Gradient method (CG) to minimize the liquid. These minimized configurations are referred to as inherent structure configurations. At low temperature region inherent structure energy ( $E_{IS}$ ) varies with temperature ( $T$ ) as:  $E_{IS} = a - \frac{b}{T}$ . Although this relation holds well at high density, this nature deviates for the lowest density  $\rho = 0.681$ . The fitted data (along with fitting parameters) are plotted for all densities.  $E_{IS}$  is calculated by averaging over 12 samples at each temperature and density.

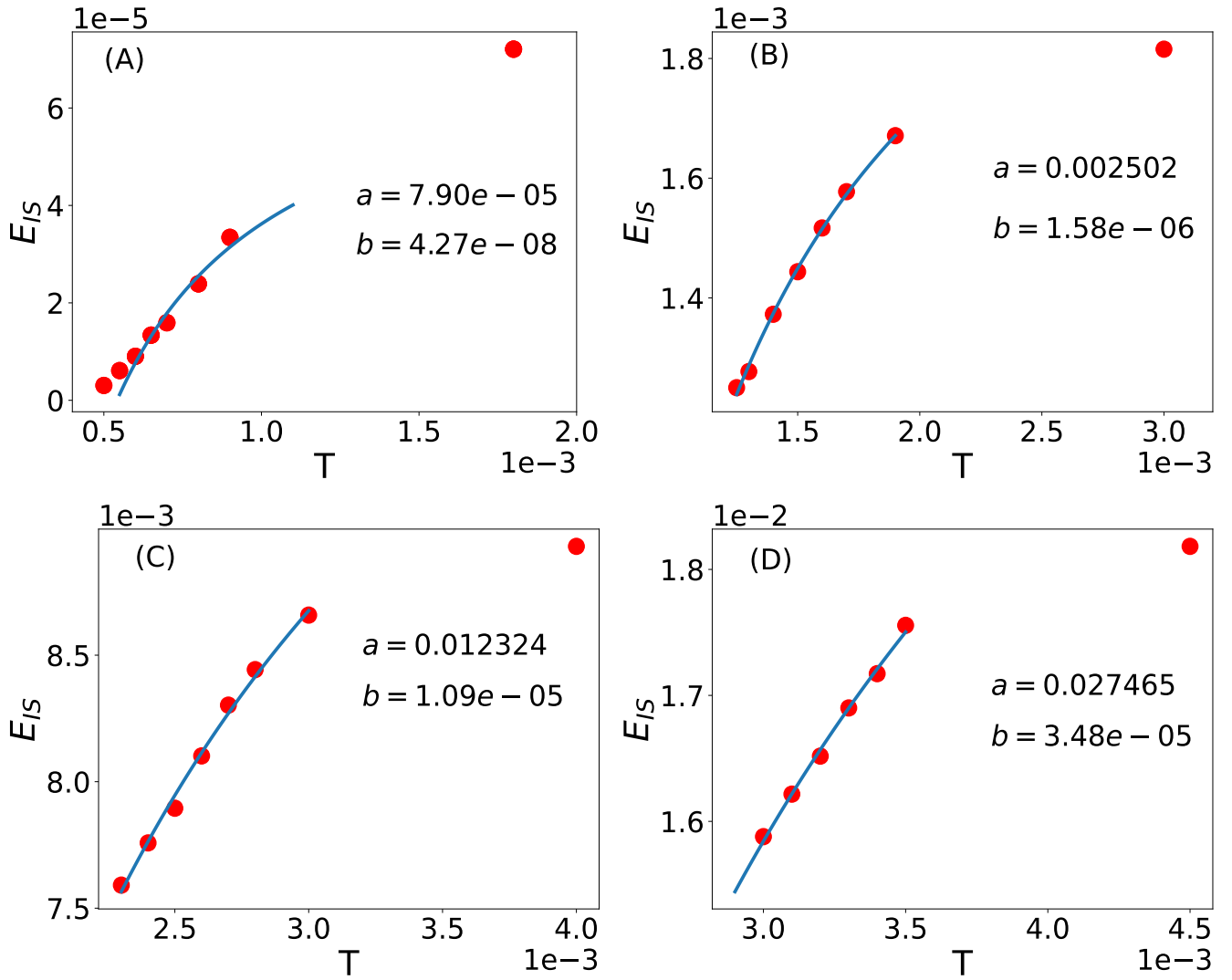


FIG. S3. Plot of inherent structure energy  $E_{IS}$  against temperature  $T$  for densities (A)  $\rho = 0.681$ , (B)  $\rho = 0.750$ , (C)  $\rho = 0.8556$ , (D)  $\rho = 0.943$ . Each curve is fitted at low temperatures via the equation:  $E_{IS} = a - b/T$ . Only for the lowest density  $\rho = 0.681$ ,  $E_{IS}$  shows deviation from  $1/T$  behaviour.

#### $T_{MCT}$ FOR DIFFERENT DENSITY

As discussed in the main text, we observe a change in shear response behavior around the Mode Coupling temperature. Here, we show how we compute  $T_{MCT}$  for different densities. According to the Mode-Coupling theory, relaxation time ( $\tau_\alpha$ ) with temperatures ( $T$ ) is well described by a power-law form:  $\tau_\alpha = \tau_0(T - T_{MCT})^{-\gamma}$ , where  $\tau_\alpha$  diverges at a critical temperature  $T_{MCT}$ . In Fig. S4, we illustrate  $\tau_\alpha$  of the liquids as a function of  $T$  along with MCT fits, and the corresponding fitted  $T_{MCT}$  is also indicated within the figures. Each panel represents a specific  $\rho$ .

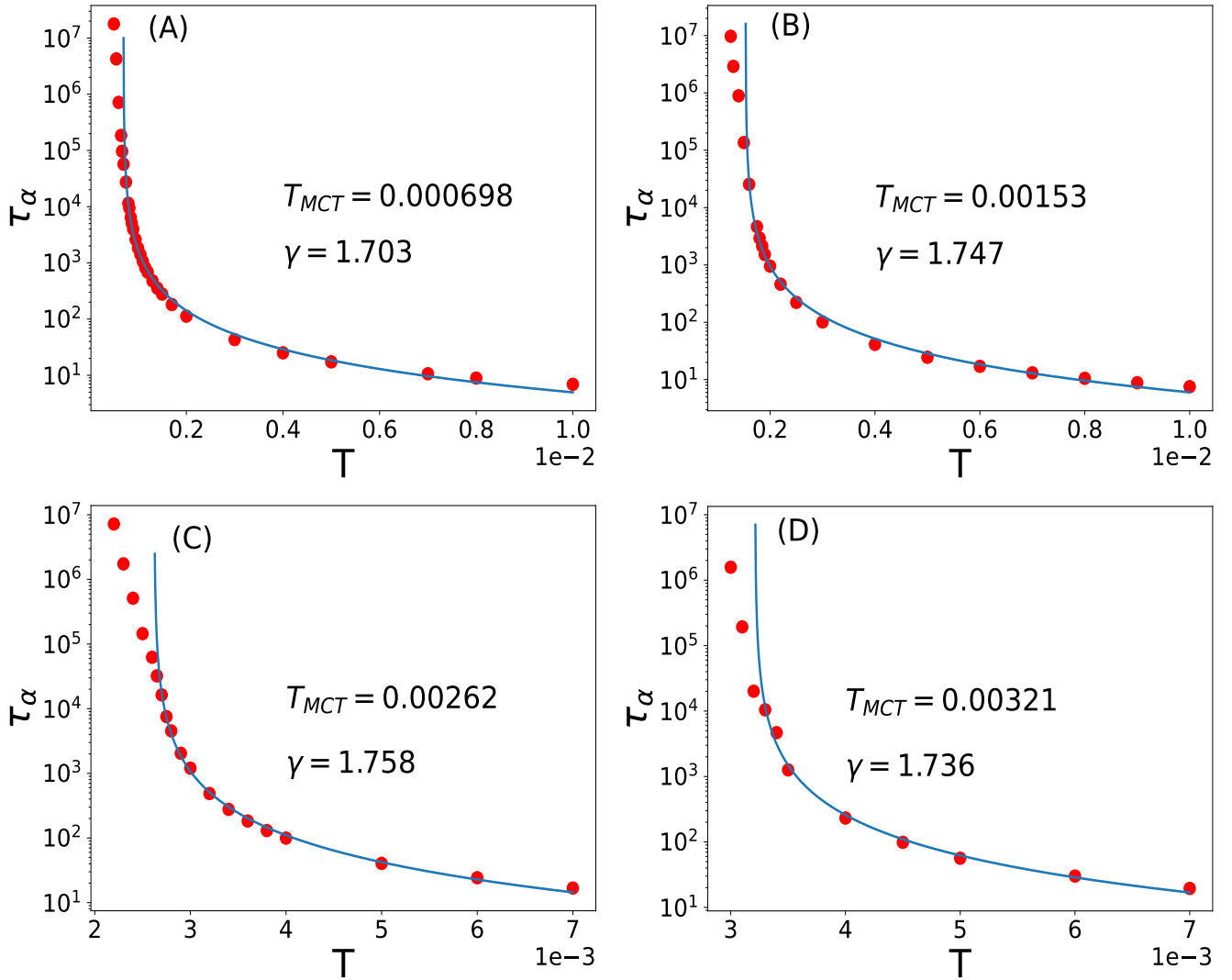


FIG. S4. Plots of  $\tau_\alpha$  extracted from the overlap function  $q(t)$ , shown as a function of the temperature  $T$  on a semi-logarithmic scale, for densities (A)  $\rho = 0.681$ , (B)  $\rho = 0.750$ , (C)  $\rho = 0.8556$ , (D)  $\rho = 0.943$ . Each curve is fitted by equation :  $\tau_\alpha = \tau_0(T - T_{MCT})^{-\gamma}$ .  $T_{MCT}$  is shown for all  $\rho$  for system size  $N = 5000$ .

### STROBOSCOPIC ENERGY WITH CYCLES AT DIFFERENT DENSITIES

Next, we show how the stroboscopic energy,  $E(\gamma = 0)$ , evolves with the number of oscillatory shear cycles. Two extreme temperature cases — highest  $T$  (represent poorly annealed glass) and lowest  $T$  (well-annealed glass)—are considered within the studied temperature range for each  $\rho$ . Stroboscopic energy obtained from  $T = 0.0018$  and  $T = 0.0005$  at  $\rho = 0.681$  are plotted for different values of strain amplitude ( $\gamma_{max}$ ) in Fig S5. At the lowest density ( $\rho = 0.681$ ), stroboscopic energies do not reach a perfect steady state even after thousands of cycles for a few  $\gamma_{max}$  in the poorly annealed case. Therefore, we fitted the  $E(\gamma = 0)$  vs  $N_{cycle}$  data using the stretched exponential relation:  $E(N_{cycle}) = E_0 + b \exp\left(-\left(\frac{N_{cycle}}{\tau}\right)^\beta\right)$  to extract the steady-state energies as well as the relaxation time,  $\tau$ , representing the number of cycles to reach the steady state. The solid lines represent the fitted data. From the fitting, we can extract  $\tau$ , the relaxation time shown in the main text. Similarly, the variation of stroboscopic energies with cycles at different  $\gamma_{max}$  for the poorly annealed and well-annealed cases are also shown for  $\rho = 0.750, 0.8556, 0.943$  in Fig. S6, S7, S8 respectively.

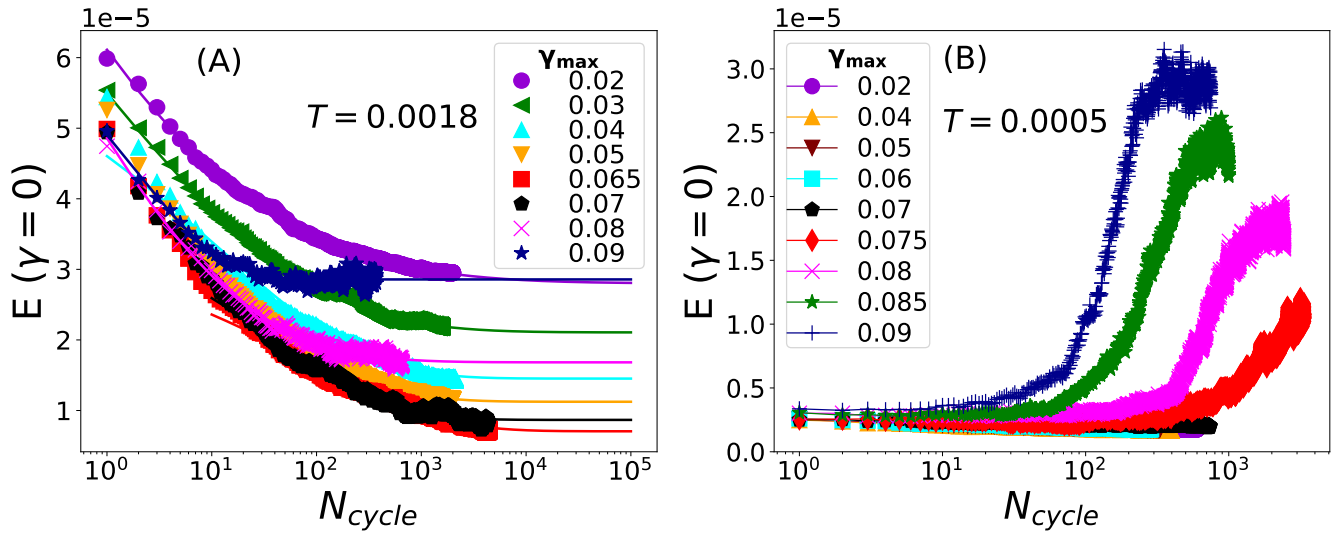


FIG. S5. Plot of stroboscopic energies with cycles at different  $\gamma_{max}$  at density  $\rho = 0.681$  for (A) poorly annealed ( $T = 0.0018$ ) and (B) well annealed ( $T = 0.0005$ ). The data are averaged over 12 samples for the system size  $N = 5000$ . Solid lines through the data set are fits to stretched exponential form. From fitting, we get the yield point is  $\gamma_y \sim 0.065$  for the poorly annealed case. The yielding transition of the well-annealed sample is at  $\gamma_y \sim 0.075$ .

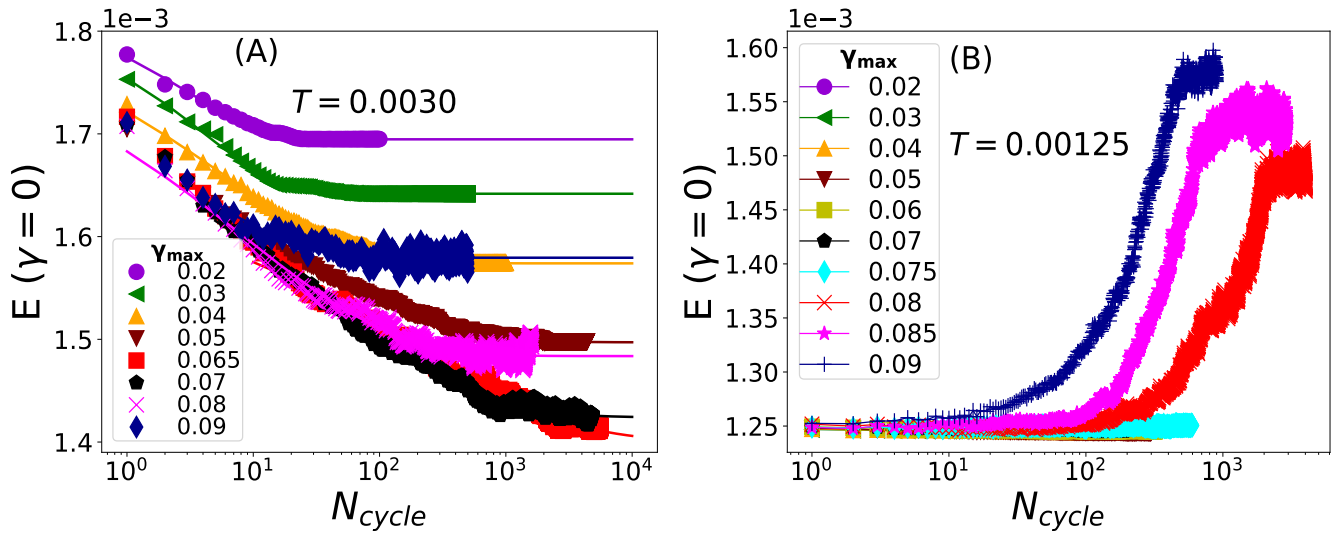


FIG. S6. Plot of stroboscopic energies with cycles at different  $\gamma_{max}$  at density  $\rho = 0.750$  for (A) poorly annealed ( $T = 0.0030$ ) and (B) well annealed ( $T = 0.00125$ ). From fitting, we get the yield point of poorly annealed is at  $\gamma_y \sim 0.065$ . The yielding is at  $\gamma_y \sim 0.08$  for the well-annealed case.

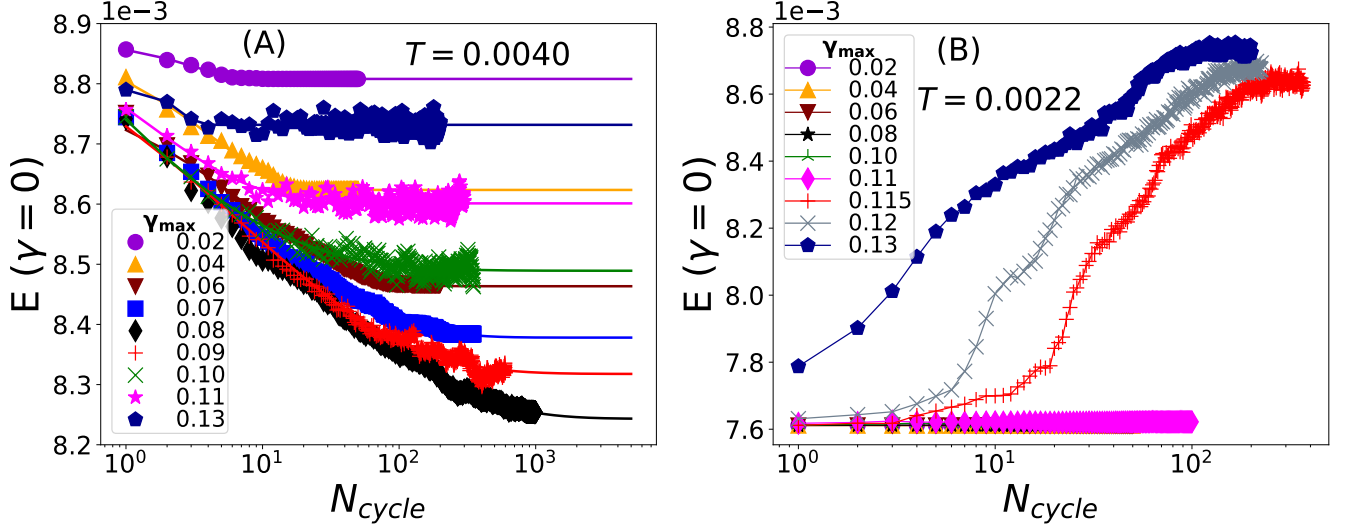


FIG. S7. Plot of stroboscopic energies with cycles at different  $\gamma_{max}$  at density  $\rho = 0.8556$  for (A) poorly annealed ( $T = 0.0040$ ), (B) well annealed ( $T = 0.0022$ ). The yield points of the poorly annealed and well-annealed cases are at  $\gamma_y \sim 0.085$  and  $\gamma_y \sim 0.115$ , respectively.

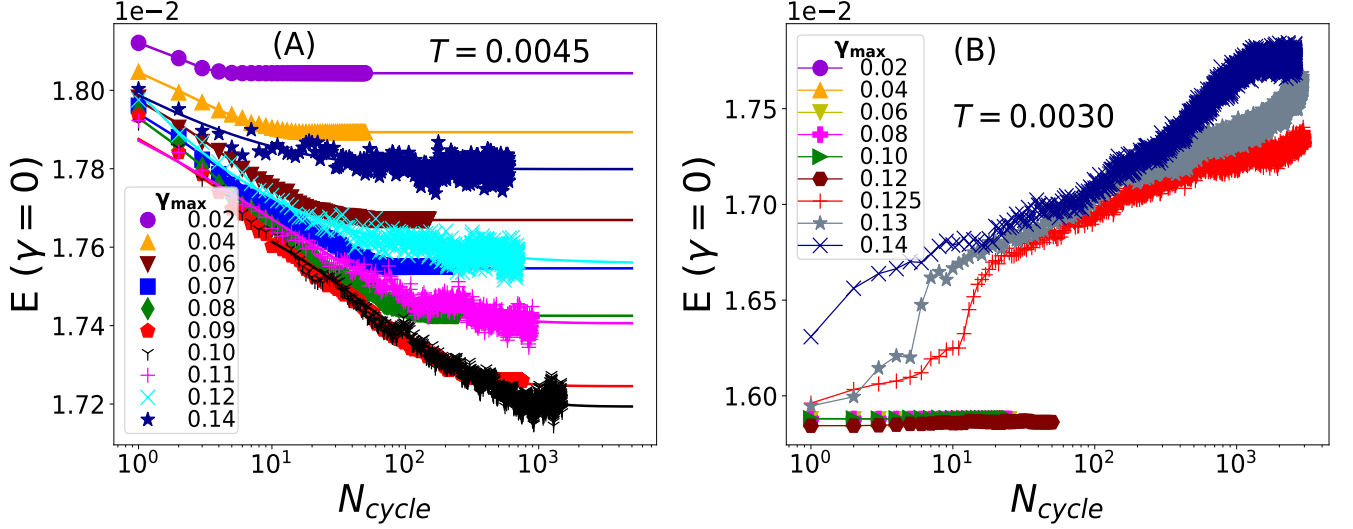


FIG. S8. Plot of stroboscopic energy vs cycles at different  $\gamma_{max}$  at density  $\rho = 0.943$  for (A) poorly annealed ( $T = 0.0045$ ), (B) well annealed ( $T = 0.0030$ ) and their corresponding yielding is at  $\gamma_y \sim 0.095$  and  $\gamma_y \sim 0.125$  respectively.

### TIMESCALE TO REACH THE STEADY STATE

Now, we show the relaxation time,  $\tau$ , obtained from the fitting described above as a function of  $\gamma_{max}$ . As  $\gamma_{max}$  approaches the yield point  $\gamma_y$ , the relaxation time to reach the steady state diverges. Although various mechanisms have been proposed in the literature to explain how  $\tau$  increases with  $\gamma_{max}$ , we have observed that  $\tau = a(\gamma_y - \gamma_{max})^{-b}$  describes our data well. In Fig. S9, we show the relaxation time as a function of  $\gamma_{max}$  for different densities, where the line represents the fit and the points represent the actual data from the simulation. Similar behaviour is also observed, as discussed in the main text for the elastoplastic model we studied. The corresponding data is shown in Fig. S10.

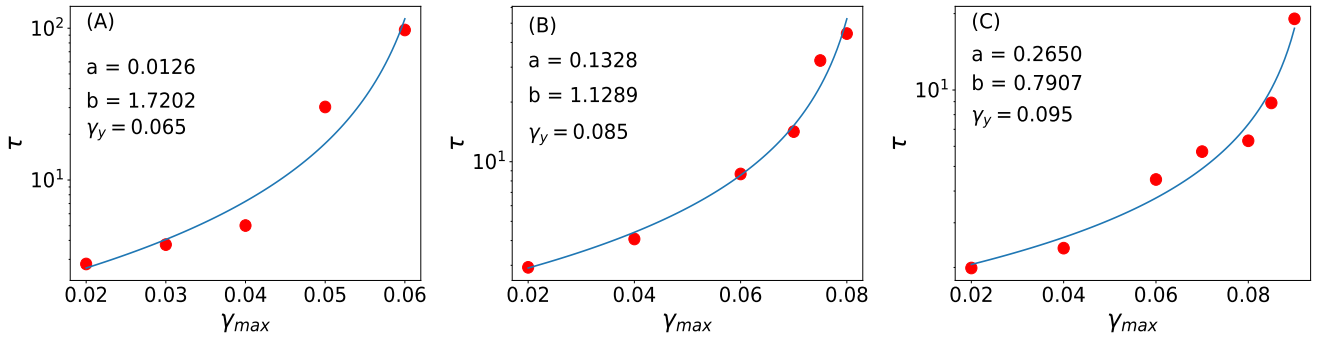


FIG. S9. Simulation: Relaxation time  $\tau$  to reach the steady state for different  $\gamma_{max}$  for (A)  $\rho = 0.750$ , (B)  $\rho = 0.8556$ , (C)  $\rho = 0.943$ . Red dots correspond to actual data, and the lines are the fit to the data.

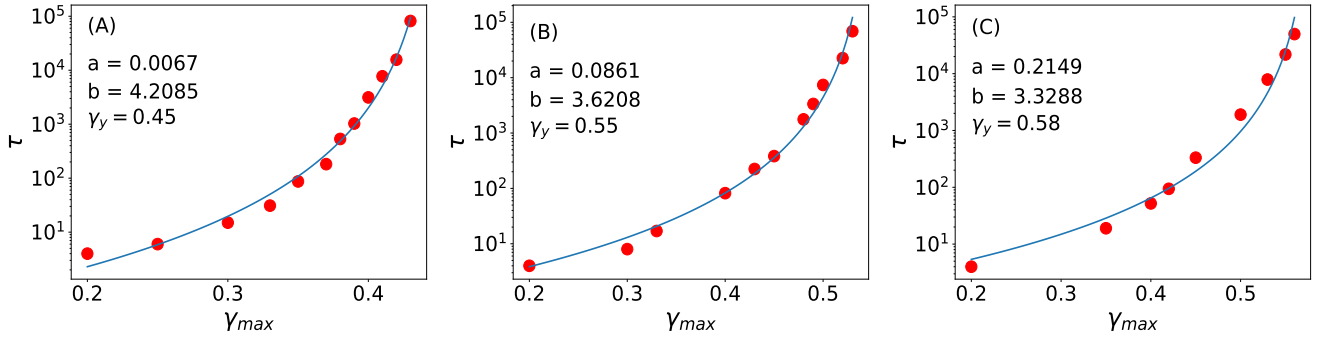


FIG. S10. Model: Number of cycles required to reach the steady state for different  $\gamma_{max}$  for (A) strong, (B) intermediate, (C) fragile case. Red dots correspond to actual data, and the lines are the fit to the data.